Catalysis Today 394-396 (2022) 414–424

Contents lists available at ScienceDirect

Catalysis Today

journal homepage: www.elsevier.com/locate/cattod

Ruthenium isomorphic substitution into manganese oxide octahedral molecular sieve OMS-2: Comparative physic-chemical and catalytic studies of Ru *versus* abundant metal cationic dopants

Ferran Sabaté, José Luis Jordà, María J. Sabater *

Instituto de Tecnología Química, Universitat Politècnica de València – Consejo Superior de Investigaciones Científicas, Avinguda dels Tarongers, s/n, 46022 València, Spain

ARTICLE INFO

Keywords:
Manganese dioxide
Octahedral molecular sieve
Ruthenium
Isomorphic substitution
Alcohol oxidation

ABSTRACT

A fraction of structural Mn cations have been replaced by different cationic dopants (*i.e.* earth abundant cationic dopants and heavier, Ru^{3+}) in the cryptomelane oxide K-OMS2. Then, a comparative study has been addressed in order to understand the relationship between physic-chemical properties and catalytic activity in this series of doped oxides. The most striking effect of doping was the weakening of the Mn-O bond so that oxygen atoms can be more easily removed from the surface layer, facilitating the production of oxygen vacancy defects (OVDs), which are key for certain catalytic applications. This weakening of the Mn—O bond was more pronounced for the case of ruthenium doped cryptomelane [Ru]-K-OMS2 oxide, which was the most active catalyst (TON = 145) during the oxidation reaction of benzyl alcohol to benzaldehyde. This feature has been correlated with the reducibility according to TPR-H_2 data and a more weakened Mn—O bond force constant value, $k_{Mn\text{-}O}$ ($N{\cdot}m^{-1}$), which varied from 301.7 to 291.8 $N{\cdot}m^{-1}$ for undoped K–OMS2 and [Ru(2%)]-K-OMS2 respectively. All the doping processes enhanced the alcohol conversion (*ca.* 2–50%) giving a high selectivity (>99%) towards the aldehyde.

1. Introduction

Manganese oxide-based materials present a high grade of polymorphism. Indeed, different phases (α, β, γ,.) with different crystal structures, morphologies, porosities and textures can be associated to a wide variety of properties [1], so depending on them they will be used in different applications. Among these uses, it is worth mentioning their use as electronic devices for energy store (capacitors and batteries) [2–7], medical treatments [8–10], fundamental material for optical devices [11–13] and for environmental control purposes among other [14–23].

In particular, octahedral molecular sieves (OMS) are getting significant attention for their easily synthesis method, thermodynamic stability and high catalytic activity [24–29]. One of the most noteworthy is the cryptomelane oxide OMS2. Cryptomelane is a crystalline microporous Mn-based oxide with a well-defined 2 × 2 tunnel structure composed primarily by manganese (III) and manganese (IV) cations located in octahedral positions with a six-coordination that causes the network to have a negative charge that needs being balanced by K^+ ions. These cations are occupying tunnel positions eight-coordinated with edge and shared MnO_6 units. Interestingly, the tunnel dimensions are (4.6 × 4.6 × 6.5) Å and they can also contain water molecules. In general, counter cations such as K^+ and water molecules are in the tunnels to provide charge balance and to stabilize the structure.

Due to the particular chemical composition and stability that provides a three-dimensional structure such as this one, attention has been paid to modify typical parameters such as particle size and morphology in order to improve its performance as a catalyst [30–32]. Another way of altering electronic, catalytic and structural properties of these materials is incorporating different metal ions as metal dopants (*i.e.* Ni, Co, Fe, Ru, …) [30,33–40]. The doping processes can occur on the surface of the solid, in the tunnels or into the structure. The last one occurs through a Mn cation replacement process called isomorphic substitution [36,41] which can cause a redistribution of oxidation states of Mn and/or the generation of vacancies in the framework in order to maintain the electroneutrality of the system [42].

Manganese oxides have numerous catalytic applications. However, the incorporation of different metal cationic dopants in their structure

* Corresponding author.
E-mail address: mjsabate@itq.upv.es (M.J. Sabater).

https://doi.org/10.1016/j.cattod.2021.06.033
Received 19 March 2021; Received in revised form 4 June 2021; Accepted 25 June 2021
Available online 9 July 2021

can provide new interesting properties due to the modifications produced in the lattice [30,36,43,44]. In this work, we have studied the replacement of a fraction of structural manganese by different metal cations in the manganese molecular sieve K–OMS2 in order to get a series of structural analogues and a comparative study has been undertaken. We have recently incorporated ruthenium into the framework of cryptomelane K-OMS2 ([Ru]-K-OMS2) [36], and in the present work we have studied the influence of Ru loading on catalytic activity when this cation is part of the K-OMS2 structure. Besides, a comparative study between Ru supported on K-OMS2 (RuO_x/K-OMS2) and a series of isomorphic cryptomelane materials doped with a large variety of metal cations (M-K-OMS2; M = Ni^{2+}, Co^{2+}, Fe^{3+}, Cu^{2+}) [30,36,45,46] was devised to correlate the variation of physic-chemical properties of the M-K-OMS2 with their catalytic activity.

2. Material and methods

2.1. Catalyst preparation

Potassium permanganate (≥99.9%, $KMnO_4$), manganese sulfate monohydrate (≥99.9%, $MnSO_4{\cdot}H_2O$) were supplied by Sigma–Aldrich (Merck) and Probus S.A, respectively. Nitric acid 65.0% technical grade was purchased from Panreac.

Metal precursor salts: cobalt(II) nitrate hexahydrate (≥98.0%, $Co(NO_3)_2.6H_2O$), copper(II) sulfate pentahydrate (≥98.0%, $Cu(SO_4){\cdot}5H_2O$), nickel(II) sulfate hexahydrate (≥98.0%, $Ni(SO_4){\cdot}6H_2O$) and iron (II) sulfate heptahydrate (≥99.0%, $Fe(SO_4){\cdot}7H_2O$) were supplied by Sigma-Adrich (Merck). Ruthenium(III) chloride hydrate (40.7%, $RuCl_3{\cdot}xH_2O$) was provided by. Johnson Mathey. All chemicals were used as received without further purification.

Cryptomelane (K-OMS2) was synthesized according to the procedure described in the literature [26,27] 2.29 g of potassium permanganate (0.014mols) in 40 mL of Milli-Q water was added to a solution of 3.52 g of manganese sulphate monohydrate (0.021 mols) in 12 mL of Milli-Q water and 1.2 mL nitric acid (65%). The solution was refluxed at 100ºC for 24 h. The final solution was centrifuged to remove the solvent and the solid was washed with water until neutral pH, being dried at 100ºC overnight. A black solid was obtained.

[Ru]-K-OMS2 was synthesized following a procedure described in the literature [36]: 2.29 g of potassium permanganate (0.014mols) in 40 mL of Milli-Q water was added to a solution of 3.52 g of manganese sulphate monohydrate (0.021 mols) in 12 mL of Milli-Q water and 1.2 mL nitric acid (65%). Then, ruthenium(III) chloride hydrate was added to the solution. The amount of ruthenium(III) chloride incorporated was: 29.9 mg, 89.7 mg, 120 mg, and 180 mg in order to get materials with 0.5%, 1.5%, 2.0%, and 4.0% wt. of ruthenium, respectively. The solutions were refluxed at 100 ºC for 24 h. The final solutions were centrifuged to remove the solvent and the solids were washed with water until neutral pH, being dried at 100ºC overnight. Black solids were obtained in all cases.

Cobalt (Co), copper (Cu), iron (Fe) and nickel (Ni) cobalt doped cryptomelane were prepared by following synthetic procedures described in the literature from their respective precursor metal salts [30,46]. The solids obtained were noted as [M]-K-OMS2 where M = Co, Cu, Fe and Ni. Theoretical metal loading in all prepared catalysts was 2% by weight of metal.

2.2. Sample characterization

The catalysts prepared were examined by atomic emission spectroscopy (ICP-AES), power X-ray diffraction (XRPD), temperature-programmed reduction (TPR-H_2), CO_2 adsorption, UV–visible and Raman spectroscopy.

The chemical composition of the samples was measured by Inductively Coupled Plasma-Atomic Emission Spectroscopy (ICP-AES) analysis. These analyses were carried out in a Varian 715-ES ICP Optical Emission spectrometer, after dissolving the solid in HNO_3/HCl (1:3) + H_2O_2/H_2SO_4 aqueous solution.

The crystal structure of the as-prepared samples was verified by X-ray powder diffraction. X-ray powder diffraction (XRPD) data of the doped and undoped cryptomelane samples were collected using a PANalytical CUBIX X-ray diffractometer with Cu Kα radiation and fixed divergence slits in the 2θ range from 10° to 100°.

H_2-TPR (temperature programmed reduction) profiles were obtained using Autochem 2910 with a thermal conductivity detector (TCD). Among forty-fifty milligrams of solid (granulometry: 0.4–0.8 mm) were placed in a quartz tube, heated to 105 °C and purged with argon gas (Ar) for 30 min, and then reduced in a stream of a mixture of 10% H_2/Ar (50.01 mL/min) at a heating rate of 5 °C/min to 600 °C.

Textural properties were obtained from the CO_2 adsorption isotherms measured at 273 K fitting the results with Dubinin–Astakhov equation and using a Micromeritics ASAP 2010 apparatus.

Raman measurements were taken at room temperature with a 785 nm laser excitation with a Renishaw Raman Spectrometer ("in *via*") equipped with a CCD detector. Before recording each spectrum, the spectrometer was calibrated with a silicon wafer.

UV–visible absorption data were collected on Cary 50 Bio UV–visible spectrophotometer. Quartz cells of 1 cm optical path length were employed for all measurements. Samples were prepared by ultrasonically dispersing an amount of the desired solid in MilliQ water. After that, an aliquot of this suspension was taken being diluted in MilliQ water in order to get a concentration of 0.19 g/L or 0.06 g/L.

The morphology of the samples was studied using a JEOL 2100F microscope operating at 200 kV both in transmission (TEM) and scanning-transmission mode (STEM). STEM images were obtained using a High Angle Annular Dark Field detector (HAADF), which allows Z-contrast imaging. Samples were prepared by dropping the suspension of the catalyst using CH_2Cl_2 as the solvent directly onto holey-carbon-coated nickel or copper grids. SEM images were recorded with a ZEISS Ultra-55 and a ZEISS Auriga-Compact field-emission scanning electron microscope operating at an accelerating voltage of 2 kV. Energy-dispersive X-ray spectroscopy (EDX) was performed with an Oxford LINK ISIS system connected to a JEOL 6300 electron microscope with the SEMQUANT program, which introduces ZAF correction. The counting time for each analysis was 100 s. Also EDX (Energy-dispersive X-ray spectroscopy) was performed connected to a JEOL 2100F and using the same software. The solid powder sample was adsorbed on conductive carbon tape.

The surface composition and the oxidation state of ruthenium and manganese were determined by X–ray photoelectron spectroscopy (XPS) with a SPECS spectrometer equipped with a 150 Magnetic Circular Dichroism (MCD) – 9 Phoibos detector and using a monochromatic Al Kα (1486.6 eV) X-ray source. Spectra were recorded using analyser pass energy of 30 eV, an X-ray power of 0 W and under an operating pressure of 10^{-9} mbar. During data processing, BE values were referenced to C1s peak (284.5 eV). Spectra treatment was performed using the CASA software.

2.3. Catalytic tests

The reactions were carried out at 110ºC and 5 bar O_2 within a reactor equipped with a microsampling system which allowed the extraction of reaction samples at regular reaction times. Under typical reaction conditions, 0.3 mmol (32 mg) benzyl alcohol, 1 mL toluene and the proper amount of catalyst were charged into the reactor. *n* – dodecane was used as internal standard. Before the reaction, the reactor was purged with oxygen up to 10 times being finally pressurized at 5 bar. The reaction was monitored by gas chromatography using an HP-5 capillary column (5% phenylmethylsiloxane, 30 m × 320 μm × 0.25 μm). Products were identified by GC–MS using an Agilent 6890N8000 equipped with a mass spectrometry detector (Agilent 5973N quadrupole detector).

Table 1
Chemical composition of K-OMS2 and [Ru]-K-OMS2 materials obtained by ICP-AES.

Material	K (%)[a]	Mn (%)[a]	Ru (%)[a,b]	Ru/Mn (molar ratio)	K/ (Mn+Ru+K) mass ratio	Mn/ (Mn+Ru+K) mass ratio
K-OMS2	5.23	71.0	–	–	–	–
[Ru(0.5%)]-K-OMS2	5.17	71.6	0.337	0.003	0.067	0.929
[Ru(1.5%)]-K-OMS2	5.04	70.4	1.37	0.010	0.066	0.917
[Ru(2%)]-K-OMS2	5.20	70.8	2.34	0.018	0.066	0.904
[Ru(4%)]-K-OMS2	5.10	68.9	3.61	0.028	0.066	0.880

[a] % weight of each element.
[b] determined also by EDX.

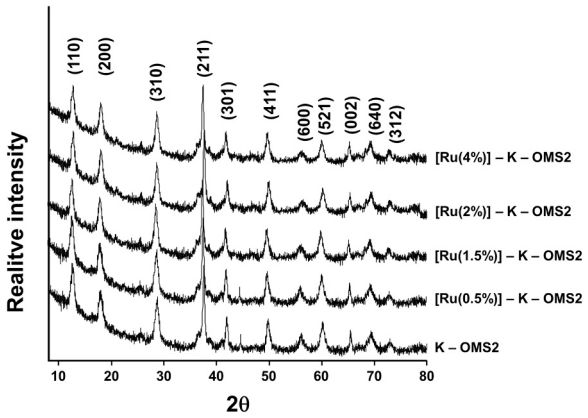

Fig. 1. XRPD diffractograms of undoped K-OMS2 and ruthenium doped materials, [Ru]-K-OMS2 with different ruthenium contents: 0.5%, 1.5%, 2% and 4%wt. of Ru.

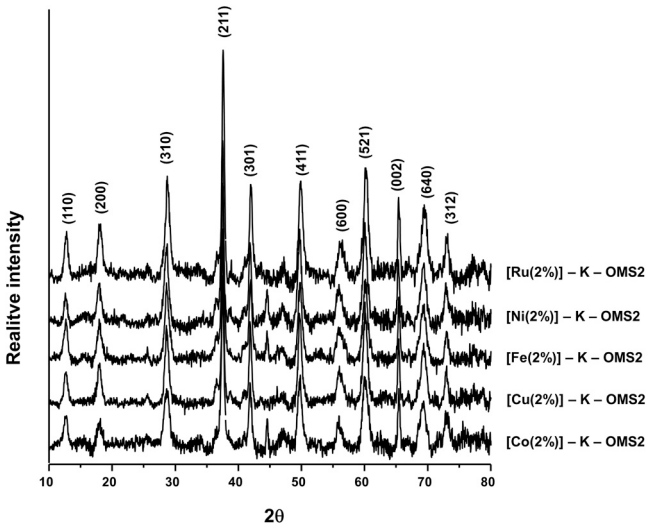

Fig. 2. XRPD diffractograms for [Cu(2%)]-K-OMS2, [Ni(%)]-K-OMS2, [Fe (2%)]-K-OMS2, [Co(%)]-K-OMS2. Diffractogram of [Ru(2%)]-K-OMS2 is also included just for comparison.

3. Results and discussion

3.1. Synthesis and characterization of doped K-OMS2 oxides

3.1.1. X-Ray powder diffraction (XRPD) and morphological characterization

A series of four Ru-doped KOMS-2 oxides with Ru loadings at 0.5% ([Ru(0.5%)]-K-OMS2), 1.5% ([Ru(1.5%)]-K-OMS2), 2.0% ([Ru(2%)]-KOMS2) and 4.0% wt. ([Ru(4%)]-K-OMS2) were synthesized through a known reflux method without using any template or any director agent [36]. The chemical composition of the as-prepared materials was analysed by Inductively Coupled Plasma-Atomic Emission spectroscopy (ICP-AES) and Energy-dispersive X-ray spectroscopy (EDX) (Tables 1 and S1).

The results included in Table 1 show the increasing incorporation of Ru in the series of doped-samples (entries 2–5). For comparative purposes, the undoped material (K–OMS2) has also been included in Table 1 (entry 1).

The results presented for the series of Ru-doped [Ru]-K-OMS2 fit with the redox exchange model proposed by Feng et al. [47], which is based on the general formula $K_xMn^{4+}_{1-x}Mn^{3+}_xO_2$ (Table S1). This model demonstrates a slight increase of the average oxidation state (AOS) (Table S1).

X–ray powder diffractograms (XRPD) were obtained for all these Ru-doped materials showing that the crystalline structure remained unchanged after the doping process across the entire range of Ru contents essayed (Fig. 1).

Indeed, as can be deduced from Fig. 1 the K–OMS2 diffraction pattern (JCPD #00–029–1020) remained basically unchanged on the entire series of Ru-doped materials both in terms of position and relative intensities of the peaks regardless of ruthenium content. At this point, it is important to note that no segregated phases related to manganese and/or ruthenium were observed in the diffractograms, so it could be concluded that all materials constituted single phases.

Nonetheless a deeper analysis of the diffractograms for the two highest Ru loadings (Ru[(2%)]-K-OMS2 and Ru[(4%)]-K-OMS2) showed an almost imperceptible shifting, *ca.* <2%, of all peaks to major 2θ values. (Fig. S1, Supporting Information). This small shifting is very relevant since it is indicative of an effective distortion of the interplanar distance (110) involving changes in the cell parameters of the oxide. We have shown in previous recent studies [36] that the incorporation of 2% wt. of ruthenium into the framework induces an expansion of the cell parameters (*a*, *b* and *c*) as for other related metallic isomorphic substitutions [30].

In parallel other isomorphic doped–cryptomelane materials were prepared using different metal cationic dopants and following known synthesis routes [30,46]. These new elements were earth abundant metal based cations (*i.e.* Ni, Co, Cu, Fe) that were incorporated to the synthesis from their respective precursor salts (see Experimental Section) to afford a series of doped-K-OMS oxides which received the following notation [Ni(2%)]-K-OMS2, [Co(2%)]-K-OMS2, [Cu (2%])-K-OMS2 and [Fe(2%)]-KOMS-2.

The resulting solids were analyzed by ICP- AES and the amount of metal cation incorporated was roughly the same in all cases (about 2% wt.), see Table S2. This series of isomorphic substituted oxides also fit with the Fengś model, according to the results published in the literature [47], and which is based in the general formula $K_xMn^{4+}_{1-x}Mn^{3+}_xO_2$.

Fig. 2 includes the diffractograms of this series of isomorphic substituted materials ([Ni(2%)]-K-OMS2, [Co(2%)]-K-OMS2, [Cu(2%)]-K-OMS2 and [Fe(2%)]-K-OMS-2) showing single phases without any segregated forms. The diffractogram of [Ru(2%)]-K-OMS2 at the same metal loading has also been included just for comparison.

Similarly and as it happened with [Ru(2%)]-K-OMS2 no relevant changes were appreciated in the structure of original cryptomelane K-

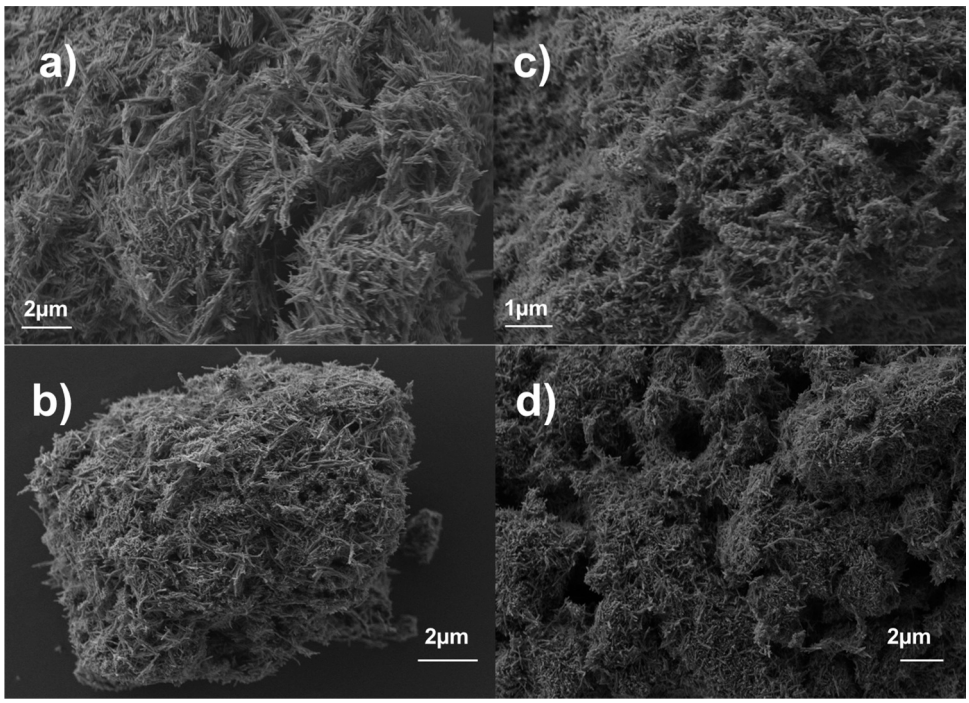

Fig. 3. SEM micrographs for [Ru]-K-OMS2 oxide with different ruthenium contents: a) 0.5%, b) 1.5%, c) 2% and d) 4% wt.

OMS2 by effect of doping hence confirming that the three dimensional structure of the original oxide was maintained.

However, unlike the previous case with Ru, no displacement of the peaks was detected in the respective diffractograms (Fig. 2). One possible explanation for the observed difference has to do with the fact that the radius of earth abundant cations (*i.e.* Co^{2+}, Cu^{2+}, Fe^{3+}, Ni^{2+}) are not much different from structural Mn (*i.e.* Mn^{3+}) [30,48], contrary to the case of the heavier cationic metal Ru^{3+}which belongs to a higher electronic level so that the incorporation of higher ionic radius into the structure would introduce a greater structural distortion in the cryptomelane lattice. In line with this result, hexavalent or pentavalent cations such as W^{6+}, Mo^{6+} or V^{5+} have shown to induce important deformations in the unit cell of cryptomelane for similar metal contents, (*i.e.* 2% wt) [49].

In reference to the morphology of the synthesized materials, an increase in crystal size was also.

observed when increasing Ru content within the series of Ru-doped oxides. For example, an increase of up to 40% in size was observed for [Ru(4%)]-KOMS2 crystals (12.7 nm) with respect.

to undoped K-OMS2 (9.1 nm) when using the Debye–Scherrer equation at $2\theta = 28.6$ Å for calculating the crystallite size. In this line, the crystal size slightly decreased (12.5 nm) when the Ru content was reduced by half in the oxide [Ru(2%)]-K-OMS2. However, there were not any significant changes in crystal size for the rest of isomorphic materials containing earth abundant cation dopants (at the same loading level) with respect to original cryptomelane, hence confirming the not appreciable variation of lattice parameters in the XRPD diffractograms within the series of earth abundant cations (Fig. 2).

With respect to composition, there is an interesting observation that has to do with the K^+ content. Effectively, taking into consideration the chemical composition of the series of Ru-doped oxides [Ru]-K-OMS2 included in Table 1, the K/(Mn+K+Metal) ratio remained constant for all cases. This was interpreted as a strong evidence in the sense that the metal substitution had not been taken place in the tunnels and the original tunnel structure remained unchanged. The same conclusion could be obtained for the series of abundant metal cations (Table S2).

Besides, two different trends were observed when looking at the Mn/(Mn + K + Metal) ratio for the two groups of materials. On the one hand, the Mn/(Mn + K + Metal) ratio dropped gradually for the series of Ru-doped oxides included in Table 1 as the Ru content increased. This was interpreted as that Mn cations were gradually being replaced by increasing amounts of Ru ions (from 0.5% to 4%wt.) in the octahedral positions of the manganese lattice. Conversely, when we look at the oxides doped with earth abundant cations (Table S2) it was possible to verify that the Mn/(Mn + K + Metal) ratio remained without significant variations in the whole series of doped oxides. This was taken as an evidence that roughly the same fraction of Mn was being replaced in this group of doped oxides (*ca.* 2%).

3.1.2. *Scanning and transmission electron microscopy*

The global morphology of K-OMS2 and Ru-doped oxides K-OMS2 was examined and compared by scanning electron and transmission electron microscopies (SEM and TEM).

In this case, ruthenium doped cryptomelane [Ru]-K-OMS2 showed a typical needle form across the entire range of Ru loadings used in this study (0.5–4%), which is the typical nanorod morphology already described for transition metal doped cryptomelane oxides [M]-K-OMS2 (M = Co, Cu, Fe and Ni) [30] (Fig. 3). The length of these thin fibers ranged from 0.15 to 0.50 μm with an average thickness up to 13 nm (by applying the Debye–Scherrer approximation) as it can be also corroborated in the Fig. S2. Interestingly, this needle shape became blurred as the Ru loading increased as can be seen in the SEM micrographs included in Fig. 3.

The amount of Ru that could be incorporated into the structure did not exceed 4%wt unlike smaller earth abundant doping cations previously mentioned, which could be incorporated in an amount close to 6% wt [30,46]. This experimental fact clearly suggests that the distortion exerted by Ru is greater than by other elements more similar in size to Mn as previously stated.

The distribution of Ru in the structure elemental mapping was studied by means of high-angle annular dark-field scanning transmission electron microscopy (HAADF–STEM) with energy-dispersive X-ray (EDX) as well as EDX-SEM was carried out on a sample containing a moderate amount of Ru ([Ru(2%)]-K-OMS2). The images clearly showed the existence of a homogeneous distribution of Ru along the entire crystal for the oxide ([Ru(2%)]-K-OMS2) (Fig. S3).

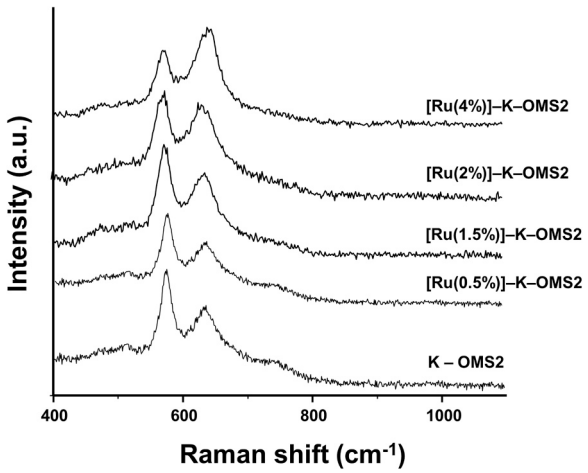

Fig. 4. Raman spectra for the undoped K-OMS2 and ruthenium doped materials [Ru(0.5%)]-K-OMS2, [Ru(1.5%)]-K-OMS2, [Ru(2%)]-K-OMS2 and [Ru (4%)]-K-OMS2.

3.1.3. *Raman spectroscopy*

To go deeper into the characterization of the Ru-doped cryptomelane K–OMS2 ([Ru(0.5%)]-K-OMS2, [Ru(1.5%)]-K-OMS2, [Ru(2%)]-K-OMS2 and Ru(4%)]-K-OMS2), they were studied by Raman spectroscopy (Fig. 4).

In principle it is reasonable to expect that the introduction of cationic dopants in the structure will have an impact on the local geometry of basic structural unities, [MnO6]-, as well as in the Mn—O bond strength [30,50]. In this regard, it has been described in the literature that according to the theory of groups, fifteen vibrational normal modes are expected to be detected for cryptomelane K-OMS2 oxide by Raman spectroscopy [50]. Nonetheless, the low polarizability and the orbital overlapping (among other physic causes) normally reduces the number of experimental normal modes to 744, 636, 577, 515, 472, 385 and 283 cm^{-1} [30,51,52]. Because of this, our study was focused on the two characteristic cryptomelane bands at 636 and 577 cm^{-1} that are related to the A1g vibrational mode type (symmetric stretching) and they reflect the degree of crystallinity of the tetragonal tunnel 2 × 2 structure [50]. Effectively, both bands at 577 and 636 cm^{-1} are associated to two different Mn-O vibrations [33]: the band at 636 cm^{-1} could be assigned to Mn–O vibrations that take place perpendicularly to the octahedron chains, whereas the band at 577 cm^{-1} can be assigned to Mn–O vibrations along the octahedron framework. Thus, when analyzing the influence of Ru content in the series of Ru-doped K-OMS2 oxides by Raman spectroscopy is possible to appreciate how the maximum of these two main bands barely move, although the relative intensity of these two bands changed in the two samples with the highest Ru content (2% and 4% wt.) (Fig. 4) [50,51]. No vibrations belonging to RuO_2 (at 1860 cm^{-1}) species were observed in the spectra [53], hence discarding the presence of segregated phases or extraframework Ru species, a fact that reinforces the purity of the whole series of oxides doped with Ru.

Since, in principle, the incorporation of Ru into the K-OMS2 lattice will influence the Mn—O—Mn bond, attempts were made to quantify the magnitude of this interaction from a *semiempirical* point of view. This was achieved by calculating the Mn–O force constant (k) for these materials on the bases of the Hookeś Law according to the following expression [54,55]:

$$\tilde{\nu} = \frac{1}{2\pi c}\sqrt{\frac{k}{\mu}} \Longrightarrow k = \mu\cdot(2\pi\cdot\tilde{\nu}\cdot c\cdot c)^2 \quad (1)$$

where $\tilde{\nu}$ is the Raman shift (cm^{-1}), c is light velocity and μ is the effective mass. Thus, the Hook's law was applied to calculate the constant $k_{Mn\text{-}O}$ ($N\cdot m^{-1}$) from the band at 636 cm^{-1} for the series of Ru-doped oxides (Fig. 5).

The results included in Fig. 5 shows that increasing incorporation of Ru into the oxide K-OMS2 causes a linear decrease in the Mn–O bond

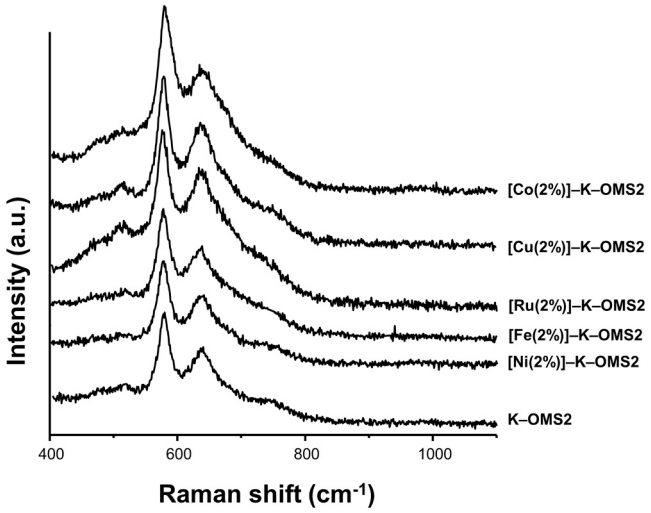

Fig. 6. Raman spectra of [Co(2%)]-K-OMS2, [Cu(2%)]-K-OMS2, [Ni(2%)]-K-OMS2, [Fe(2%)]-K-OMS2 and [Ru(2%)]-K-OMS2.

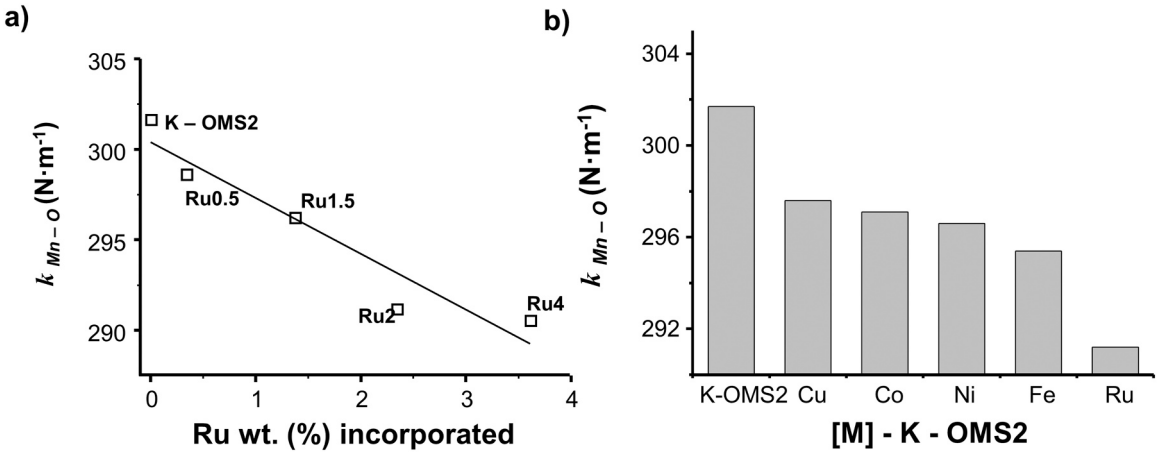

Fig. 5. Graphic representation of $k_{Mn\text{-}O}$ ($N\cdot m^{-1}$) obtained for: a) K-OMS2 and [Ru]-doped oxides: [Ru(0.5%)]-K-OMS2, [Ru(1.5%)]-K-OMS2, [Ru(2%)]-KOMS2 and [Ru(4%)]-K-OMS2 (Ru0.5, Ru1.5, Ru2, Ru4) and b) for [M(2% wt.)]-K-OMS2, where M = Cu, Co, Ni, Fe and Ru.

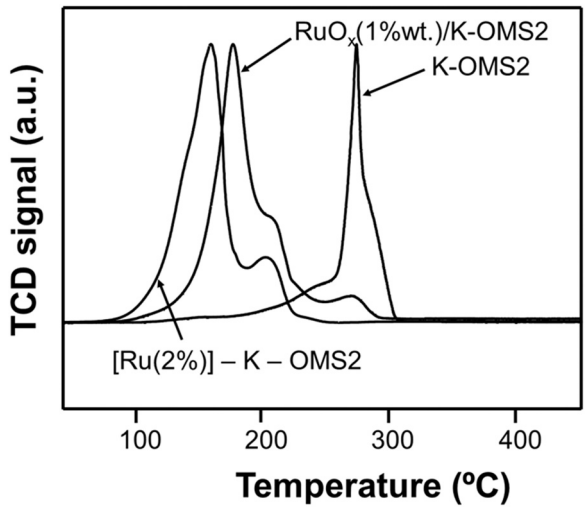

Fig. 7. H_2 – TPR profiles: K–OMS2, [Ru(2%)]–K–OMS2 and RuO_x (1% wt.)/K-OMS2.

strength, since $k_{Mn\text{-}O}$ ($N{\cdot}m^{-1}$) experienced a gradual decrease which was totally dependent on the amount of Ru incorporated (Fig. 5a).

In this case, the lowest $k_{Mn\text{-}O}$ ($N{\cdot}m^{-1}$) value was obtained for the oxide with the highest Ru content [Ru(4%)]-K-OMS2).

This result is highly important in the sense that Ru[(4%)]-K-OMS2 can be predicted to be the most reactive sample among all.

For comparison purposes, the set of Raman spectra was obtained for the series of isomorphic substitutions with earth abundant cations mentioned above (Fig. 6).

In this case the main widened bands at 637 and 577 cm^{-1} were again observed in all cases but displacement was barely appreciated in any case. Similarly, vibrations belonging to the respective oxides (*i.e.* CuO, NiO, CuO, and Fe_2O_3.) were not observed in the spectra, hence confirming the formation of single phases. The $k_{Mn\text{-}O}$ ($N{\cdot}m^{-1}$) values were also calculated for these doped oxides. (Fig. 5b and Table S3) and according to them (Fig. 5b), it can be concluded that isomorphic substitution led to a decrease of the $k_{Mn\text{-}O}$ ($N{\cdot}m^{-1}$) value following this order: K-OMS2 > Cu > Co > Ni > Fe > Ru. This means that Ru produces the greatest weakening of the Mn—O bond since it has the lowest $k_{Mn\text{-}O}$ value (*ca.* 291 $N{\cdot}m^{-1}$).

This should be due to the larger size of Ru with respect to Mn (and earth abundant cations) that can presumably cause the greatest distortion in the cryptomelane structure. For this same reason it may be expected that changes in physic-chemical properties [30,35,37,44,46,49,52,56] should be more marked for isomorphically Ru-doped oxides, than for the other metal doped samples.

3.1.4. *UV-Vis spectroscopy*

The effect of doping processes can also be evaluated by means of UV–visible spectroscopy. Fig. S4 shows that pure K-OMS2 and [Ru(2%)]-K-OMS2 have a broad absorptive region from 300 to 600 nm in their respective UV-Vis spectra. This absorption can be attributed to *d-d* transitions of manganese ions [50,57] and thus it has been commonly found for most of doped manganese oxides. Interestingly [Ru(2%)]-K-OMS2 showed a much more intense absorption than K-OMS2, and this was interpreted as due to an improvement of charge transfer processes. In this case, the absorption band was blue-shifted after incorporating Ru^{3+} (*ca.* 448 nm). [36,43]. When the UV-Vis spectra of the rest of doped materials was analysed a displacement to more energetic transitions were also observed although not as markedly as with Ru (Fig. S5). In this case, an increase in the respective absorption bands was also observed indicating that charge transfer processes are also favoured, as previously indicated.

3.1.5. *TPR-H_2 study*

The remarkable weakening that Mn-O bond experiences, especially when incorporating Ru^{3+} (Section 3.1.3), should be reflected in different variables and physic–chemical properties of the solids, such as the trend to reducibility. For this reason, H_2 - TPR (Temperature-Programmed Reduction) studies were also carried out on the entire series of doped solids.

The reducibility of pure K-OMS2 as well as isomorphic substituted [Ru(2%)]-K-OMS2 had already been compared by means of H_2 -TPR (Temperature-Programmed Reduction) [36]. In this case, the H_2-TPR of a Ru impregnated sample (RuO_x(1%)/K-OMS2) was also studied for comparison. RuO_x(1.0%)/K-OMS2 was prepared by contacting K-OMS2 with an aqueous solution containing $RuCl_3.xH_2O$ under vigorous stirring, followed by filtration, drying and calcination in air [36]. In this case, the ruthenium content of Ru impregnated K-OMS2 (RuO_x(1%)/-K-OMS2) was similar to that found for the outermost layers of cryptomelane [Ru(2%)]-K-OMS2 obtained through XPS spectroscopy (Table S4).

Fig. 7 includes the most interesting results obtained by TPR-H_2 with these two Ru containing oxides at the surface and at the structural level. The TPR data from the original undoped cryptomelane K-OMS2 are also

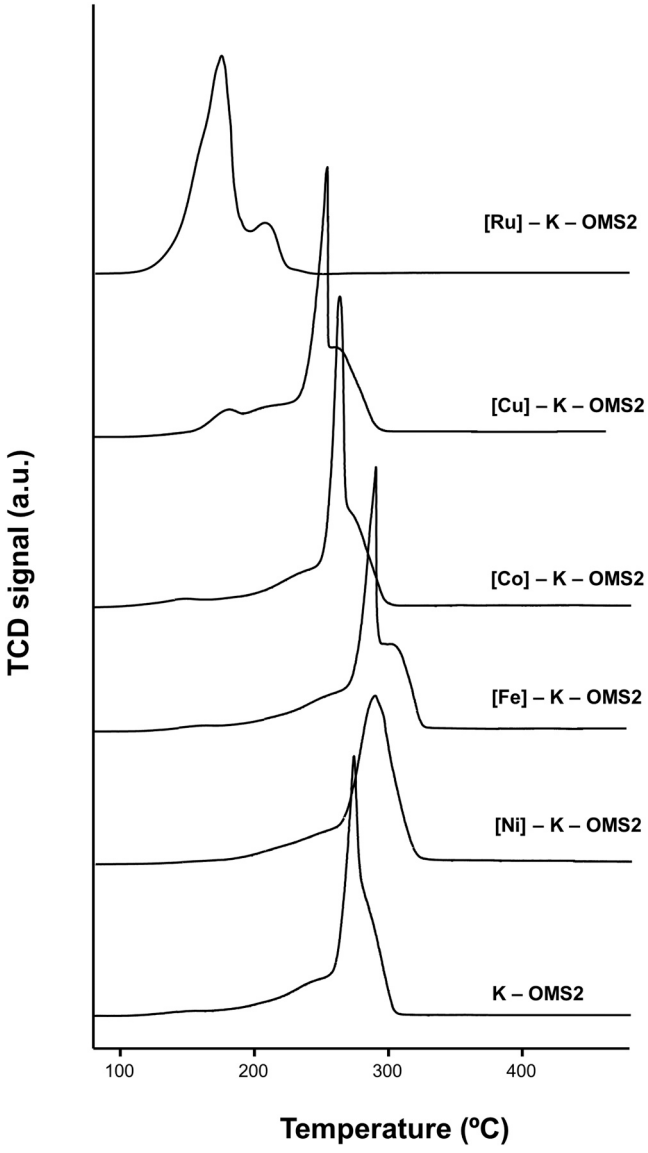

Fig. 8. H_2 – TPR profiles for [Co(2%)]-K-OMS2, [Cu(2%)]-K-OMS2, [Fe(2%)]-K-OMS2, [Ni(2%)]-K-OMS2, [Ru(2%)]-K-OMS2 and K-OMS2 oxides.

included for comparison.

The results showed that K-OMS2 presented a unique band around 271ºC that could be decomposed into different overlapping bands and a shoulder around 245ºC. All these components were clearly assigned to the reduction of structural Mn^{4+} and Mn^{3+} cations involving different phase changes [58–61]:

$$MnO_{2\ (s)} \rightarrow Mn_2O_{3\ (s)} \rightarrow Mn_3O_{4\ (s)} \rightarrow MnO_{\ (s)} \quad (2)$$

Then, the incorporation of ruthenium into the structural lattice and at superficial level ([Ru(2%)]-K-OMS2 and RuO_x (1% *wt.*)/K-OMS2 respectively) had a strong influence on the TPR profiles because in both cases, a remarkable displacement of the bands at lower temperatures could be appreciated (Fig. 7).

Effectively, from these results it was observed that the incorporation of ruthenium into the structural lattice had a strong influence on the TPR profile since [Ru(2%)]-K-OMS2 showed a much greater displacement of the bands at lower temperatures (at 160º and 204ºC) than when Ru was placed at the surface level (RuO_x(1%)/K-OMS2) (Fig. 7).

In this context, it was foreseeable that the surface level deposition of RuO_x on the K-OMS2 oxide could have a less marked influence on the reducibility of the resulting material RuO_x(1%)/K-OMS2 than when Ru was placed at structural level, as in fact it could be deduced from Fig. 7.

It is important to indicate that the typical reduction band of Ru^{4+} species bound to oxygenated supports (*i.e.* alumina, titania) were not detected in neither of this two doped samples provided that this process has been reported to occur around 275ºC according to literature references [62–66].

Interestingly the peak at 160ºC could be assigned tentatively to reduction of structural Mn cations under the influence of the dopant agent, similar to what happens with the incorporation of other elements [37,58–61,67]. From the above TPR-H_2 results it follows that the major effect that Ru exerts on the cryptomelane lattice as a dopant is increase the reducibility of the oxide; a fact that is more pronounced when Ru is forming part of the framework. This result agrees with the noticeably weakening of the Mn-O bond observed in previous Raman experiments and that will be decisive in catalysis (Section 3.2).

Then, a TPR–H_2 study of the series of oxides doped with metal cations of fourth period [45,59,68], [Co(2%)]-K-OMS2, [Cu(2%)]-K-OMS2, [Fe(2%)]-K-OMS2 and [Ni(2%)]-K-OMS2 was carried out (Fig. 8). For comparative purposes the TPR-H_2 of K-OMS2 and [Ru(2%)]-K-OMS2 has also been included in the figure.

As seen in Fig. 8, excepting for the case of Ni and Fe, which induced the reduction of the respective doped oxides at slightly higher temperatures than undoped K-OMS2, the cationic dopants Co, Cu and Ru favored the reducibility of K-OMS2 since in these cases, a remarkable displacement of the bands at lower temperatures could be appreciated being the most pronounced effect for the case of Ru.

Results especially for the case of Ni and Fe appear to introduce an extra-stabilization on the system and deviate from what is predicted by the Mn-O bond strength on the bases of the $k_{Mn\text{-}O}$ ($N{\cdot}m^{-1}$) constant (Section 3.1.3). This experimental fact can be explained if we take into account that reduction processes in TPR-H_2 studies may involve not only phase changes but also formation of highly stable species by reaction with certain cationic dopants (*i.e.* formation of allotropic oxides forms in the case of Ni and Fe) [69,70]. These highly stable species would consume an extra amount of H_2 therefore preventing this correlation from taking place in the case of Fe and Ni.

3.2. Catalytic activity

In order to study the influence of changes in physic-chemical properties on catalytic activity, the series of isomorphic substituted cryptomelane K-OMS2 oxides above described were applied as heterogeneous catalysts in the oxidation reaction of alcohols to aldehydes.

Traditionally, oxides of cryptomelane type K-OMS2 have been used as catalysts in oxidation reactions provided their recognized ability to exchange oxygen. This ability has been closely related to the presence of oxygen vacancy defects (OVD) in the solid, which are key for certain catalytic applications and whose formation can be enhanced through doping processes as it has extensively been reported in the literature [58, 71–75].

Scheme 1. Oxidation reaction of benzyl alcohol to benzaldehyde using molecular oxygen as oxidant catalysed by undoped and transition metal-doped cryptomelane K-OMS2 catalysts.

Table 2
Oxidation reaction of benzyl alcohol to benzaldehyde in the presence of undoped K-OMS2 and K-OMS2 doped with different cations (2% wt.).

Entry[a]	Catalyst	Conv. (%)[b]	Yield (%)[c]	TON[d]/ TOF[e]	r_0 (mmol·h^{-1})
1	[Ru(2%)]-K-OMS2	82	82	145/181	0.358
2	[Co(2%)]-K-OMS2	75	75	39/81	0.295
3	[Cu(2%)]-K-OMS2	71	71	49/82	0.211
4	[Ni(2%)]-K-OMS2	58	58	42/51	0.180
5	[Fe(2%)]-K-OMS2	55	55	35/48	0.166
6	K-OMS2	54	54	-/-	0.083
7	Blank	0	0	–	–

[a] 0.25 mmol benzyl alcohol, 8–10 mg of catalyst (~25% by weight), 1 mL de toluene *n* – dodecane (internal standard), T = 110 ºC, p_{O2} = 5 bar, 7 h.
[b] Conversion (%) was obtained by gas chromatography (GC) on the basis of alcohol converted.
[c] Yield (%) of benzaldehyde was obtained by GC on the basis of alcohol converted and benzaldehyde obtained.
[d] TON is calculated as mmols of alcohol converted/mmols of Ru
[e] TOF: calculated as rate of formation of benzaldehyde/mmol of Ru. [f] (-): this value does not apply.

Thus, since OVDs are in principle good descriptors for the ability of oxides to participate in oxidation reactions, and given that the synthesis of aldehydes and ketones from alcohols are relevant industrially [76–85], we have used the oxidation of benzyl alcohol to benzaldehyde as model reaction to carry out this study (Scheme 1).

For this reason, [Ru(2%)]-K-OMS2 and the complete series of cryptomelane oxides doped with different cations were all tested as catalysts in the oxidation of benzyl alcohol and the most relevant catalytic results are included in Table 2.

According to the results included in Table 2, all cryptomelane – type materials were active under smooth reaction conditions. They showed a high selectivity towards obtaining the aldehyde, since no secondary products were detected in any case by gas chromatography (GC). In addition, mass balances were completed for all cases, whereas control reactions showed that there was no conversion in the absence of any catalysts (entry 7, Table 2), showing that the latter was absolutely essential to carry out the reaction.

According to these results, [Ru(2%)]-K-OMS2 was the most active catalyst since it gave the maximum initial reaction rate value (r_0) and the highest yield of the desired product benzaldehyde (entry 1, Table 2).

Table 3
Oxidation reaction of benzyl alcohol to benzaldehyde catalyzed by undoped K-OMS2 and Ru-doped materials.

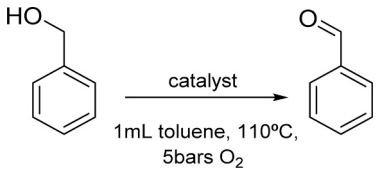

Entry[a]	Catalyst	Ru content (%mmol)	Conversion (%)[c]	Yield (%)[d]	Mass Balance (%)	TON[e]/TOF[f]	r_0 (mmol·h^{-1})
1	[Ru(2%)]-K-OMS2	0.5	82	82	100	145/181	0.358
2[b]	[Ru(2%)]-K-OMS2	0.5	19	19	100	35/34	0.133
3	[Ru(0.5%)]-K-OMS2	0.1	64	64	100	488/208	0.103
4	[Ru(1.5%)]-K-OMS2	0.4	75	75	100	128/187	0.252
5	[Ru(4%)]-K-OMS2	1.0	100	100	100	64/56	0.222
6	RuO_x(1%wt)/K-OMS2	0.5	61	61	100	133/84	0.095
7[b]	RuO_x(1%wt)/K-OMS2	0.5	7	7	100	16/13	0.032
8	RuO_x (2%wt)/K-OMS2	0.8	68	68.0	95.0	88/50	0.094
9	K-OMS2	–	54	54	100	–	0.083
10[b]	K-OMS2	–	14	14	100	–	0.007
11	RuO_x/Al_2O_3	0.5	9	6	96	22/11	n.d
12	RuO_x/ZrO_2	0.4	17	12	95	41/32	n.d
13	RuO_x/TiO_2	0.5	15	8.0	94	32/18	n.d

[a] 0.25 mmol benzyl alcohol, 8–10 mg of catalyst (~25% by weight), 1 mL de toluene *n* – dodecane (internal standard), T = 110 ºC, p_{O2} = 5 bar, 7 h.
[b] Reaction carried out under inert atmosphere (p_{N2} = 3.5–4.0 bar).
[c] Conversion (%) was obtained by gas chromatography (GC) on the basis of alcohol converted.
[d] Yield (%) of benzaldehyde was obtained by GC on the basis of alcohol converted and benzaldehyde obtained.
[e] TON is calculated as mmols of alcohol converted/mmols of Ru.
[f] TOF: calculated as rate of formation of benzaldehyde/mmol of Ru. (-): this value does not apply; n.d.: undetermined.

Besides, [Ru(2%)]-K-OMS2 gave the highest TON/TOF values among the series of doped oxides essayed. Indeed, these TOF/TON values were 3 and even 4 times higher than those obtained with the rest of abundant metal cations used as dopants (see Table 2).

This improved catalytic data in the case of [Ru(2%)]-K-OMS2 was accompanied by the best reducibility data obtained through TPR-H_2 studies (Section 3.1.5) as well as by semi-empirical data regarding the force constant value $k_{Mn\text{-}O}$ (Section 3.1.3). In fact, this parameter points out that Mn—O bond in the [Ru(2%)]-K-OMS2 oxide is the one that has been weakened the most within the entire series of oxides under study.

However, although in general all doped materials showed a higher activity than undoped K-OMS2 (entries 1–6, Table 2), a direct correlation could not be found with semi-empirical data regarding the force constant value (Section 3.1.3). A plausible explanation has to do with the apparent lability introduced by doping regarding the formation of structural defects (among them oxygen vacancy defects, OVD). Indeed they can be created during the dopant incorporation and later readjustment of the structure in order the keep the stability and/or electroneutrality of the system [51], and these structural defects are not reflected in the Hooke's Law (from which the force constant value $k_{Mn\text{-}O}$ is obtained). Nonetheless, although this correlation could not be established, a general trend was observed in the sense that the incorporation of a cationic dopant induced a weakening of the Mn—O bond in the whole series of doped oxides and this resulted in an increase of the reaction rate with respect to undoped K-OMS2 (see Tables 2 and S4).

From these results, we focused on ruthenium as cationic dopant in K-OMS2 materials. In this case the series of K-OMS oxides doped with different Ru loadings were used as catalysts in the oxidation reaction: [Ru(0.5%)]-K-OMS2, [Ru(1.5%)]-K-OMS2, [Ru(2%)]-K-OMS2 and [Ru (4%)]-K-OMS2.

For comparative purposes, RuO_x was also deposited on different supports and the results are also included in Table 3.

From these results, all the materials were active in the oxidation reaction of benzyl alcohol to benzaldehyde and mass balances were practically completed in most cases (Table 3).

Regarding the series of Ru-doped cryptomelane oxides, it was observed that increasing the Ru loading in the series of K-OMS oxides led to an increase in the yield of the desired product benzaldehyde. Indeed, maximum conversion, selectivity and yield values towards benzaldehyde could be achieved in detrimental of TON/TOF values with the highest Ru content, [Ru(4%)]-KOMS2 (see entries 1–5, Table 3).

Moreover, an increase in the initial reaction rate r_0 was observed in the series of isomorphically Ru-doped oxides by increasing the amount of Ru until reaching a maximum at 2%wt Ru (entries 1, 3–5, Table 3). However, an increase of the Ru loading (4% wt.) led to a slight decrease (*ca.* 4%) of reaction rate.

This result sharply contrasts with the $k_{Mn\text{-}O}$ trend for the series of Ru-doped oxides, which predicted that Ru[(4%)]-K-OMS2 would be the most reactive Ru-doped oxide as it had the lowest $k_{Mn\text{-}O}$ value (Section 3.1.3). This seemingly contradictory fact can be explained if we take into account that it is rather plausible that the structural positions into which Ru is progressively entering are not equivalent.

Besides, since it has been suggested that oxygen atoms bound simultaneously to Mn and Ru (Mn–O–Ru) are more reactive than when they are exclusively bonded to Mn [36], the increase in reactivity could be associated with an increase in the formation of Mn–O–Ru species. Then, from a certain amount of Ru, other less reactive species associated with Ru may begin to form and reactivity would decrease (*i.e.* Ru–O–Ru).

As can be deduced from Table 3 (entries 1–10), Ru doping both structurally and superficially.

improve the catalytic results (up to 85%). From these facts, some kind of cooperative effect between Mn and Ru species can be deduced; so to confirm this hypothesis the catalytic activity of Ru on other different supports was analysed. Catalytic studies were extended to other Ru doped catalysts using Al_2O_3, ZrO_2 and TiO_2 as solid supports (entry 11–13, Table 3). All of these catalysts were prepared with a Ru content of 1 *wt%* and using an impregnation method, followed by filtration and calcination in air [36].

It is very important to note that in all these cases the catalytic activity was inferior to that observed for the series of Ru-doped cryptomelane materials (see entries 1–5 and entries 11–13 in Table 3).

These results confirmed the importance of the Ru/Mn pair into the structure of cryptomelane for catalytic activity. Indeed this reinforced the previous observation regarding the formation of Mn–O–Ru species at the surface of K-OMS2, as the main responsible for the activity [36],

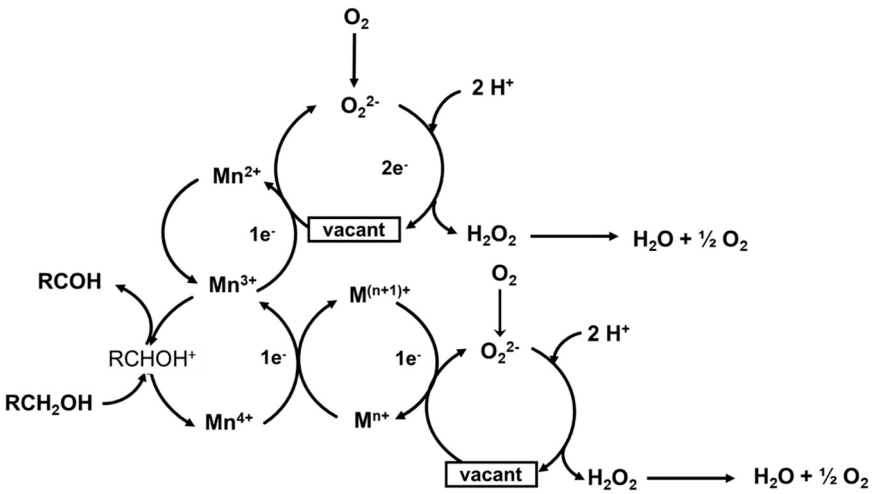

Fig. 9. Proposed reaction mechanism for the oxidation of benzyl alcohol to benzaldehyde in the presence of doped [M(2%)]-K-OMS-2 as a catalyst [36].

Heterogeneity of the catalysis was also proved by means of hot filtration experiments that indicated that reaction occurred only on the surface and not by lixiviated species in the liquid whereas reusability experiments allowed to extent the performance of [Ru(2%)]-K-OMS2 up to three uses after a regeneration process. Induced–coupled plasma (ICP) analyses and XRPD diffractograms had already shown that crystal structure remained unchangeable after this recovery process [36].

Regarding the reaction mechanism, it was shown that oxidation reaction of benzyl alcohol to benzaldehyde occurred through a Mars–van-Krevelen mechanism with undoped and Ru-doped K-OMS2 as catalysts [36,86–88]. In this case it was proposed that the reaction would start with the involvement of the oxygen lattice in the oxidation reaction, being the framework later reoxidized by molecular oxygen [36,86–88]. In other words, in a first stage the organic substrate would be oxidized and the metal would undergo a two-electron reduction from Mn^{4+} to Mn^{2+} as depicted in the Fig. 9.

In that particular case, the role of metallic cationic dopant (Ru) was restricted to reoxidize manganese reduced species to Mn^{3+} and Mn^{4+} and maintain the neutrality. This hypothesis seemed plausible given that XPS measurements [36] done for [Ru(2%)]-K-OMS2 showed (Table S4) that the manganese oxidation states practically did not vary after use, whereas a decrease in Ru^{4+} species and an increase in Ru^{3+} were observed by XPS once the reaction was completed.

More in-depth studies are necessary to complete the mechanism in the case of other metal cationic dopants, but by analogy a plausible role might be, at least in part, to attend the redox pair Mn^{3+}/Mn^{4+} during the oxidation of alcohols in order to keep the electro neutrality of the structure.

4. Conclusion

The physic-chemical properties of cryptomelane-type material K-OMS-2 have been modified by replacing a fraction of the structural Mn cations by different cationic dopants (*i.e.* Co, Ni, Fe, Cu and Ru) to get a series of structural analogues denoted as [Co(2%)]-K-OMS2, [Cu(2%)]-K-OMS2, [Fe(2%)]-K-OMS2, [Ni(2%)]-K-OMS2 and [Ru(2%)]-K-OMS2.

By combining spectroscopic and analytic techniques (X-ray diffraction, Raman, electron microscopy, H_2 – temperature programmed), we could prove that the whole series of doped materials were synthesized as single phases.

All this series of doped oxides improved the oxidation of benzyl alcohol to benzaldehyde with respect to the original undoped K-OMS2, being highly selective towards the formation of reaction product. Among them, [Ru(2%)]-K-OMS2 was the most promising catalyst for this reaction. Moreover, an increase in the amount of structural Ru resulted in an increase in the conversion values which reached 100(%) with a Ru content of 4% ([Ru(4%)]-K-OMS2).

Interestingly, when the cationic dopant was similar in size to Mn (*i.e.* Fe, Co, Ni and Cu) a direct correlation between Mn—O strength with catalytic activity could not be easily established because a number of parameters come into play that have a similar influence on catalytic activity. However, when the cationic dopant was significantly different from Mn (as is the case of Ru) the trends observed from reducibility data and Mn—O bond strength, $k_{Mn\text{-}O}$, were clear and unambiguous and could be correlated with activity. As an example, a weakening in the Mn—O bond of about 4% led to a 50% improvement in catalytic activity.

CRediT authorship contribution statement

Ferran Sabaté: Methodology, Investigation, Writing – original draft. **Jose Luis Jordá**; Methodology, Investigation; **María J. Sabater**: Conceptualization, Supervision, Investigation, Funding acquisition.

Declaration of Competing Interest

The authors declare that they have no known competing financial interests or personal relationships that could have appeared to influence the work reported in this paper.

Acknowledgements

Financial support by Ministerio de Ciencia e Innovación through the Severo Ochoa Program (SEV 2016–0683) and Ministerio de Ciencia Innovación y Universidades, Programa Estatal de Generación de Conocimiento (PGC2018-101247-B-100) are gratefully acknowledged.

F.S. acknowledges to Ministerio de Ciencia, Innovación y Universidades (Gobierno de España) for the economic support through Ayuda Predoctoral FPI – Severo Ochoa.

Appendix A. Supporting information

Supplementary data associated with this article can be found in the online version at doi:10.1016/j.cattod.2021.06.033.

References

[1] H. Chen, Y. Wang, Y.-K. Lv, Catalytic oxidation of NO over MnO_2 with different crystal structures, RSC Adv. 6 (2016) 54032–54040.

[2] F. Cheng, J. Zhao, W. Song, C. Li, H. Ma, J. Chen, P. Shen, Facile controlled synthesis of MnO_2 nanostructures of novel shapes and their application in batteries, Inorg. Chem. 45 (2006) 2038–2044.

[3] Z. Zhang, F. Xiao, S. Wang, Hierarchically structured MnO_2/graphene/carbon fiber and porous graphene hydrogel wrapped copper wire for fiber-based flexible all-solid-state asymmetric supercapacitors, J. Mater. Chem. A 3 (2015) 11215–11223.
[4] C. Xu, F. Kang, B. Li, H. Du, Recent progress on manganese dioxide based supercapacitors, J. Mater. Res. 25 (2010) 1421–1432.
[5] W. Guo, C. Yu, S. Li, Z. Wang, J. Yu, H. Huang, J. Qiu, Strategies and insights towards the intrinsic capacitive properties of MnO_2 for supercapacitors: challenges and perspectives, Nano Energy 57 (2019) 459–472.
[6] D.A. Tompsett, S.C. Parker, M.S. Islam, Surface properties of α-MnO_2: relevance to catalytic and supercapacitor behaviour, J. Mater. Chem. A 2 (2014) 15509–15518.
[7] N.R. Chodankar, D.P. Dubal, G.S. Gund, C.D. Lokhande, Flexible all-solid-state MnO_2 thin films based symmetric supercapacitors, Electrochim. Acta 165 (2015) 338–347.
[8] X. Li, X. Zhang, W. Zhang, L. Li, W. Gao, X. Zhang, D. Gao, Biocatalysis of MnO_2-mediated nanosystem for enhanced multimodal therapy and real-time tracking, ACS Sustain. Chem. Eng. 8 (2020) 13206–13214.
[9] Y. Chen, D. Ye, M. Wu, H. Chen, L. Zhang, J. Shi, L. Wang, Break-up of two-dimensional MnO_2 nanosheets promotes ultrasensitive pH-triggered theranostics of cancer, Adv. Mater. 26 (2014) 7019–7026.
[10] T.G. Spiro, J.R. Bargar, G. Sposito, B.M. Tebo, Bacteriogenic manganese oxides, Acc. Chem. Res. 43 (2010) 2–9.
[11] H. Jia, N. Li, S. Li, J. Liu, Y. Dong, Z. Jia, W. Di, G. Qin, W. Qin, MnO_2 nanosheets as saturable absorbers for a Q-switched fiber laser, Opt. Mater. Express 10 (2020) 3097–3106.
[12] B.A. Pinaud, Z. Chen, D.N. Abram, T.F. Jaramillo, Thin films of sodium birnessite-type MnO_2: optical properties, electronic band structure, and solar photoelectrochemistry, J. Phys. Chem. C 115 (2011) 11830–11838.
[13] A.J.A. Al-Nidawi, K.A. Matori, A. Zakaria, M.H. Mohd Zaid, Effect of MnO_2 doped on physical, structure and optical properties of zinc silicate glasses from waste rice husk ash, Results Phys. 7 (2017) 955–961.
[14] M. Gheju, I. Balcu, G. Mosoarca, Removal of Cr(VI) from aqueous solutions by adsorption on MnO_2, J. Hazard. Mater. 310 (2016) 270–277.
[15] J. Huang, S. Zhong, Y. Dai, C.-C. Liu, H. Zhang, Effect of MnO_2 phase structure on the oxidative reactivity toward bisphenol A degradation, Environ. Sci. Technol. 52 (2018) 11309–11318.
[16] J. Shan, Y. Zhu, S. Zhang, T. Zhu, S. Rouvimov, F. (Feng) Tao, Catalytic performance and in situ surface chemistry of pure α-MnO_2 nanorods in selective reduction of NO and N_2O with CO, J. Phys. Chem. C 117 (2013) 8329–8335.
[17] E. Saputra, S. Muhammad, H. Sun, H.M. Ang, M.O. Tadé, S. Wang, Different crystallographic one-dimensional MnO_2 nanomaterials and their superior performance in catalytic phenol degradation, Environ. Sci. Technol. 47 (2013) 5882–5887.
[18] H. Chen, J. He, Facile synthesis of monodisperse manganese oxide nanostructures and their application in water treatment, J. Phys. Chem. C 112 (2008) 17540–17545.
[19] G. Zhu, J. Zhu, W. Jiang, Z. Zhang, J. Wang, Y. Zhu, Q. Zhang, Surface oxygen vacancy induced α-MnO_2 nanofiber for highly efficient ozone elimination, Appl. Catal. B Environ. 209 (2017) 729–737.
[20] S. Liang, F. Teng, G. Bulgan, R. Zong, Y. Zhu, Effect of phase structure of MnO_2 nanorod catalyst on the activity for CO oxidation, J. Phys. Chem. C 112 (2008) 5307–5315.
[21] J. Cao, Q. Mao, L. Shi, Y. Qian, Fabrication of γ-MnO_2/α-MnO_2 hollow core/shell structures and their application to water treatment, J. Mater. Chem. 21 (2011) 16210–16215.
[22] D. Zhao, X. Yang, H. Zhang, C. Chen, X. Wang, Effect of environmental conditions on Pb(II) adsorption on β-MnO_2, Chem. Eng. J. 164 (2010) 49–55.
[23] K. Lin, W. Liu, J. Gan, Oxidative removal of bisphenol A by manganese dioxide: efficacy, products, and pathways, Environ. Sci. Technol. 43 (2009) 3860–3864.
[24] S.L. Brock, N. Duan, Z.R. Tian, O. Giraldo, H. Zhou, S.L. Suib, A review of porous manganese oxide materials, Chem. Mater. 10 (1998) 2619–2628.
[25] S. Suib, Sorption, catalysis and separation by design, Chem. Innov. 30 (3) (2001) 27–33.
[26] R.N. DeGuzman, Y.-F. Shen, E.J. Neth, S.L. Suib, C.-L. O'Young, S. Levine, J. M. Newsam, Synthesis and characterization of octahedral molecular sieves (OMS-2) having the hollandite structure, Chem. Mater. 6 (1994) 815–821.
[27] S.L. Suib, L.E. Iton, Magnetic studies of manganese oxide octahedral molecular sieves: a new class of spin glasses, Chem. Mater. 6 (1994) 429–433.
[28] Y. Ding, X. Shen, S. Sithambaram, S. Gomez, R. Kumar, V.M.B. Crisostomo, S. L. Suib, M. Aindow, Synthesis and catalytic activity of cryptomelane-type manganese dioxide nanomaterials produced by a novel solvent-free method, Chem. Mater. 17 (2005) 5382–5389.
[29] S.L. Suib, Porous Manganese Oxide Octahedral Molecular Sieves and Octahedral.
[30] C.K. King'ondu, N. Opembe, C. Chen, K. Ngala, H. Huang, A. Iyer, H.F. Garcés, S. L. Suib, Manganese oxide octahedral molecular sieves (OMS-2) multiple framework substitutions: a new route to OMS-2 particle size and morphology control, Adv. Funct. Mater. 21 (2011) 312–323.
[31] J.C. Villegas, L.J. Garces, S. Gomez, J.P. Durand, S.L. Suib, Particle size control of cryptomelane nanomaterials by use of H_2O_2 in acidic conditions, Chem. Mater. 17 (2005) 1910–1918.
[32] J. Yuan, W.-N. Li, S. Gomez, S.L. Suib, Shape-controlled synthesis of manganese oxide octahedral molecular sieve three-dimensional nanostructures, J. Am. Chem. Soc. 127 (2005) 14184–14185.
[33] X. Chen, Y.-F. Shen, S.L. Suib, C.L. O'Young, Characterization of manganese oxide octahedral molecular sieve (M−OMS-2) materials with different metal cation dopants, Chem. Mater. 14 (2002) 940–948.
[34] W. Sun, L. Cao, J. Yang, Conversion of inert cryptomelane-type manganese oxide into a highly efficient oxygen evolution catalyst via limited Ir doping, J. Mater. Chem. A 4 (2016) 12561–12570.
[35] C. Calvert, R. Joesten, K. Ngala, J. Villegas, A. Morey, X. Shen, S.L. Suib, Synthesis, characterization, and rietveld refinement of tungsten-framework-doped porous manganese oxide (K-OMS-2) material, Chem. Mater. 20 (2008) 6382–6388.
[36] F. Sabaté, J.L. Jordá, M.J. Sabater, A. Corma, Synthesis of isomorphically substituted Ru manganese molecular sieves and their catalytic properties for selective alcohol oxidation, J. Mater. Chem. A 8 (2020) 3771–3784.
[37] M. Ousmane, G. Perrussel, Z. Yan, J.M. Clacens, F. De Campo, M. Pera-Titus, Highly selective direct amination of primary alcohols over a Pd/K-OMS-2 catalyst, J. Catal. 309 (2014) 439–452.
[38] H.C. Genuino, Y. Meng, D.T. Horvath, C.-H. Kuo, M.S. Seraji, A.M. Morey, R. L. Joesten, S.L. Suib, Enhancement of catalytic activities of octahedral molecular sieve manganese oxide for total and preferential CO oxidation through vanadium ion framework substitution, ChemCatChem 5 (2013) 2306–2317.
[39] L. Tabassum, H. Tasnim, A.G. Meguerdichian, W.S. Willis, J. Macharia, C. Price, Y. Dang, S.L. Suib, Enhanced catalytic activity of a vanadium-doped mesoporous octahedral molecular sieve-2 (K-OMS-2) toward hydrogen evolution reaction, ACS Appl. Energy Mater. 3 (2020) 12185–12193.
[40] P. Egutko, J. Gryboś, M. Fedyna, J. Janas, A. Wach, J. Szlachetko, A. Adamski, X. Yu, Z. Zhao, A. Kotarba, Z. Sojka, Soot combustion over niobium-doped cryptomelane (K-OMS-2) nanorods—redox state of manganese and the lattice strain control the catalysts performance, Catalysts 10 (2020) 1390.
[41] S. Ching, K.S. Krukowska, S.L. Suib, A new synthetic route to todorokite-type manganese oxides, Inorg. Chim. Acta 294 (1999) 123–132.
[42] M.T. Nguyen Dinh, J.M. Giraudon, A.M. Vandenbroucke, R. Morent, N. De Geyter, J.F. Lamonier, Manganese oxide octahedral molecular sieve K-OMS-2 as catalyst in post plasma-catalysis for trichloroethylene degradation in humid air, J. Hazard. Mater. 314 (2016) 88–94.
[43] L.R. Pahalagedara, S. Dharmarathna, C.K. King'ondu, M.N. Pahalagedara, Y. T. Meng, C.H. Kuo, S.L. Suib, Microwave-assisted hydrothermal synthesis of α-MnO_2: lattice expansion via rapid temperature ramping and framework substitution, J. Phys. Chem. C 118 (2014) 20363–20373.
[44] X. Wu, X. Yu, Z. Chen, Z. Huang, G. Jing, Low-valence or tetravalent cation doping of manganese oxide octahedral molecular sieve (K-OMS-2) materials for nitrogen oxide emission abatement, Catal. Sci. Technol. 9 (2019) 4108–4117.
[45] P. Stelmachowski, A.H.A. Monteverde Videla, T. Jakubek, A. Kotarba, S. Specchia, The effect of Fe, Co, and Ni structural promotion of cryptomelane (KMn_8O_{16}) on the catalytic activity in oxygen evolution reaction, Electrocatalysis 9 (2018) 762–769.
[46] J. Cai, J. Liu, W.S. Willis, S.L. Suib, Framework doping of iron in tunnel structure cryptomelane, Chem. Mater. 13 (2001) 2413–2422.
[47] Q. Feng, H. Kanoh, Y. Miyai, K. Ooi, Alkali metal ions insertion/extraction reactions with hollandite-type manganese oxide in the aqueous phase, Chem. Mater. 7 (1995) 148–153.
[48] L. Pauling. The Nature of the Chemical Bond, third ed., Cornell University Press, Ithaca, United States, 1960.
[49] C.-H. Chen, E.C. Njagi, S.-Y. Chen, D.T. Horvath, L. Xu, A. Morey, C. Mackin, R. Joesten, S.L. Suib, Structural distortion of molybdenum-doped manganese oxide octahedral molecular sieves for enhanced catalytic performance, Inorg. Chem. 54 (2015) 10163–10171.
[50] T. Gao, M. Glerup, F. Krumeich, R. Nesper, H. Fjellvåg, P. Norby, Microstructures and spectroscopic properties of cryptomelane-type manganese dioxide nanofibers, J. Phys. Chem. C. 112 (2008) 13134–13140.
[51] L. Yang, J. Ma, X. Li, C. Zhang, H. He, Enhancing oxygen vacancies of Ce-OMS-2 via optimized hydrothermal conditions to improve catalytic ozone decomposition, Ind. Eng. Chem. Res. 59 (2020) 118–128.
[52] M. Polverejan, J.C. Villegas, S.L. Suib, Higher valency ion substitution into the manganese oxide framework, J. Am. Chem. Soc. 126 (2004) 7774–7775.
[53] A. Korotkov, H. Ying-Sheng, T. Kwong-Kau, T. Dah-Shyang, Raman scattering characterization of well-aligned RuO_2 and IrO_2 nanocrystals, J. Raman Spectrosc. 38 (2007) 737–749.
[54] J. Hou, Y. Li, L. Liu, L. Ren, X. Zhao, Effect of giant oxygen vacancy defects on the catalytic oxidation of OMS-2 nanorods, J. Mater. Chem. A 1 (2013) 6736–6741.
[55] J. Hou, L. Liu, Y. Li, M. Mao, H. Lv, X. Zhao, Tuning the K+ concentration in the tunnel of OMS-2 nanorods leads to a significant enhancement of the catalytic activity for benzene oxidation, Environ. Sci. Technol. 47 (2013) 13730–13736.
[56] T. Uematsu, Y. Miyamoto, Y. Ogasawara, K. Suzuki, K. Yamaguchi, N. Mizuno, Molybdenum-doped α-MnO_2 as an efficient reusable heterogeneous catalyst for aerobic sulfide oxygenation, Catal. Sci. Technol. 6 (2016) 222–233.
[57] L.-T. Tseng, Y. Lu, H.M. Fan, Y. Wang, X. Luo, T. Liu, P. Munroe, S. Li, J. Yi, Magnetic properties in α-MnO_2 doped with alkaline elements, Sci. Rep. 5 (2015) 9094.
[58] A. Davó-Quiñonero, I. Such-Basáñez, J. Juan-Juan, D. Lozano-Castelló, P. Stelmachowski, G. Grzybek, A. Kotarba, A. Bueno-López, New insights into the role of active copper species in CuO/Cryptomelane catalysts for the CO-PROX reaction, Appl. Catal. B Environ. (2019), 118372.
[59] A. Davó-Quiñonero, M. Navlani-García, D. Lozano-Castelló, A. Bueno-López, CuO/cryptomelane catalyst for preferential oxidation of CO in the presence of H_2: deactivation and regeneration, Catal. Sci. Technol. 6 (2016) 5684–5692.
[60] W.Y. Hernández, M.A. Centeno, S. Ivanova, P. Eloy, E.M. Gaigneaux, J. A. Odriozola, Cu-modified cryptomelane oxide as active catalyst for CO oxidation reactions, Appl. Catal. B Environ. 123–124 (2012) 27–35.

[61] F. Sabaté, J. Navas, M.J. Sabater, A. Corma, Synthesis of γ-lactones from easily and accessible reactants catalyzed by Cu–MnOx catalysts, C. R. Chim. 21 (2018) 164–173.
[62] P. Betancourt, A. Rives, R. Hubaut, C.E. Scott, J. Goldwasser, A study of the ruthenium–alumina system, Appl. Catal. A Gen. 170 (1998) 307–314.
[63] A. Ananth, D.H. Gregory, Y.S. Mok, Synthesis, characterization and shape-dependent catalytic co oxidation performance of ruthenium oxide nanomaterials: influence of polymer surfactant, Appl. Sci. 5 (2015) 344–358.
[64] A. Ballarini, P. Benito, G. Fornasari, O. Scelza, A. Vaccari, Role of the composition and preparation method in the activity of hydrotalcite-derived Ru catalysts in the catalytic partial oxidation of methane, Int. J. Hydrog. Energy 38 (2013) 15128–15139.
[65] D. Wang, J. Huang, F. Liu, X. Xu, X. Fang, J. Liu, Y. Xie, X. Wang, Rutile RuO2 dispersion on rutile and anatase TiO_2 supports: the effects of support crystalline phase structure on the dispersion behaviors of the supported metal oxides, Catal. Today 339 (2020) 220–232.
[66] B. Man, H. Zhang, J. Zhang, X. Li, N. Xu, H. Dai, M. Zhu, B. Dai, Oxidation modification of Ru-based catalyst for acetylene hydrochlorination, RSC Adv. 7 (2017) 23742–23750.
[67] A. Davó-Quiñonero, D. Lozano-Castelló, A. Bueno-López, Unexpected stability of CuO/Cryptomelane catalyst under Preferential Oxidation of CO reaction conditions in the presence of CO_2 and H2O, Appl. Catal. B Environ. 217 (2017) 459–465.
[68] S. Sultana, Z. Ye, S.K.P. Veerapandian, A. Löfberg, N. De Geyter, R. Morent, J.-M. Giraudon, J.-F. Lamonier, Synthesis and catalytic performances of K-OMS-2, Fe/K-OMS-2 and Fe-K-OMS-2 in post plasma-catalysis for dilute TCE abatement, Catal. Today 307 (2018) 20–28.
[69] I.R. Leith, M.G. Howden, Temperature-programmed reduction of mixed iron—manga.
[70] V. Shadravan, V.J. Bukas, G.T.K.K. Gunasooriya, J. Waleson, M. Drewery, J. Karibika, J. Jones, E. Kennedy, A. Adesina, J.K. Nørskov, M. Stockenhuber, Effect of Manganese on the Selective Catalytic Hydrogenation of COx in the Presence of Light Hydrocarbons Over Ni/Al_2O_3: An Experimental and Computational Study, ACS Catal. 10 (2020) 1535–1547, https://doi.org/10.1021/acscatal.9b04863.
[71] B.A. Cymes, C.B. Almquist, M.P.S. Krekeler, Europium-doped cryptomelane: Multi-pathway synthesis, characterization, and evaluation for the gas phase catalytic oxidation of ethanol, Appl. Catal. A: Gen. 589 (2020), 117310.
[72] X. Zhang, Z. Ma, Z. Song, H. Zhao, W. Liu, M. Zhao, J. Zhao, Role of Cryptomelane in Surface-Adsorbed Oxygen and Mn Chemical Valence in MnOx during the Catalytic Oxidation of Toluene, J. Phys. Chem. C. 123 (2019) 17255–17264.
[73] V.P. Santos, M.F.R. Pereira, J.J.M. Órfão, J.L. Figueiredo, The role of lattice oxygen on the activity of manganese oxides towards the oxidation of volatile organic compounds, Appl. Catal. B Environ. 99 (2010) 353–363.
[74] A. Iyer, J. Del-Pilar, C.K. King'ondu, E. Kissel, H.F. Garces, H. Huang, A.M. El-Sawy, P.K. Dutta, S.L. Suib, Water Oxidation Catalysis using Amorphous Manganese Oxides, Octahedral Molecular Sieves (OMS-2), and Octahedral Layered (OL-1) Manganese Oxide Structures, J. Phys. Chem. C. 116 (2012) 6474–6483.
[75] J. Luo, Q. Zhang, J. Garcia-Martinez, S.L. Suib, Adsorptive and Acidic Properties, Reversible Lattice Oxygen Evolution, and Catalytic Mechanism of Cryptomelane-Type Manganese Oxides as Oxidation Catalysts, J. Am. Chem. Soc. 130 (2008) 3198–3207.
[76] J.S. Garcia, R.D. Harbison, Chapter 55: Aldehydes and Ketone, Hamilton & Hardy's Industrial Toxicology. Editorial Mosby. 5a Ed. (1998).
[77] British Petroleum, BP Energy Outlook. 2019 edition, United Kingdom, 2020.
[78] A.W. Cook, K.M. Waldie, Molecular Electrocatalysts for Alcohol Oxidation: Insights and Challenges for Catalyst Design, ACS Appl. Energy Mater. 3 (2020) 38–46.
[79] J.H.J. Kluytmans, A.P. Markusse, B.F.M. Kuster, G.B. Marin, J.C. Schouten, Engineering aspects of the aqueous noble metal catalysed alcohol oxidation, Catal. Today 57 (2000) 143–155.
[80] C. Parmeggiani, C. Matassini, F. Cardona, A step forward towards sustainable aerobic alcohol oxidation: new and revised catalysts based on transition metals on solid supports, Green. Chem. 19 (2017) 2030–2050.
[81] R. Ciriminna, V. Pandarus, F. Béland, Y.-J. Xu, M. Pagliaro, Heterogeneously Catalyzed Alcohol Oxidation for the Fine Chemical Industry, Org. Process Res. Dev. 19 (2015) 1554–1558.
[82] A. Dhakshinamoorthy, A.M. Asiri, H. Garcia, Tuneable nature of metal organic frameworks as heterogeneous solid catalysts for alcohol oxidation, Chem. Commun. 53 (2017) 10851–10869.
[83] M. Boronat, A. Corma, F. Illas, J. Radilla, T. Ródenas, M.J. Sabater, Mechanism of selective alcohol oxidation to aldehydes on gold catalysts: Influence of surface roughness on reactivity, J. Catal. 278 (2011) 50–58.
[84] A. Corma, S. Iborra, A. Velty, Chemical Routes for the Transformation of Biomass into Chemicals, Chem. Rev. 107 (2007) 2411–2502.
[85] C. Della Pina, E. Falletta, L. Prati, M. Rossi, Selective oxidation using gold, Chem. Soc. Rev. 37 (2008) 2077–2095.
[86] N.N. Opembe, C. Guild, C. King'ondu, N.C. Nelson, I.I. Slowing, S.L. Suib, Vapor-Phase Oxidation of Benzyl Alcohol Using Manganese Oxide Octahedral Molecular Sieves (OMS-2), Ind. Eng. Chem. Res. 53 (2014) 19044–19051.
[87] S. Young-Chan, V.D. Makwana, Y.-C. Son, A.R. Howell, S.L. Suib, Efficient, Catalytic, Aerobic Oxidation of Alcohols with Octahedral Molecular Sieves (https://doi.org/doi:), Angew. Chem. Int. Ed. 40 (2001) 4280–4283, https://doi.org/10.1002/1521-3773(20011119)40:22<4280::AID-ANIE4280>3.0.CO;2-L.
[88] V.D. Makwana, Y.-C. Son, A.R. Howell, S.L. Suib, The Role of Lattice Oxygen in Selective Benzyl Alcohol Oxidation Using OMS-2 Catalyst: A Kinetic and Isotope-Labeling Study, J. Catal. 210 (2002) 46–52.